Astronomy & Astrophysics manuscript no. ks-arxiv
November 18, 2022

Towards a resolved Kennicutt-Schmidt law at high redshift

J. Freundlich[1,⋆], F. Combes[1], L. J. Tacconi[2], M. C. Cooper[3], R. Genzel[2,4,5], R. Neri[6], A. Bolatto[7], F. Bournaud[8], A. Burkert[9], P. Cox[6], M. Davis[5], N. M. Förster Schreiber[2], S. Garcia-Burillo[10], J. Gracia-Carpio[2], D. Lutz[2], T. Naab[11], S. Newman[5], A. Sternberg[12], and B. Weiner[13]

[1] LERMA, Observatoire de Paris, CNRS, 61 av. de l'Observatoire, F-75014 Paris, France
[2] Max-Planck-Institute für extraterrestrische Physik (MPE), Giessenbachstrasse 1, 85748 Garching, Germany
[3] Dept. of Physics & Astronomy, Frederick Reines Hall, University of California, Irvine, CA 92697, USA
[4] Dept. of Physics, Le Conte Hall, University of California, CA 94720 Berkeley, USA
[5] Dept. of Astronomy, Campbell Hall, University of California, CA 94720 Berkeley, USA
[6] IRAM, 300 rue de la Piscine, F-38406 St. Martin d'Heres, Grenoble, France
[7] Dept. of Astronomy, University of Maryland, College Park, MD 20742-2421, USA
[8] CEA, IRFU, SAp, 91191 Gif-sur-Yvette, France
[9] Universitätsternwarte der Ludwig-Maximiliansuniversität, Scheinerstrasse 1, 81679 München, Germany, MPG-Fellow at MPE
[10] Observatorio Astronómico Nacional - OAN, Apartado 1143, 28800 Alcalá de Henares, Madrid, Spain
[11] Max Planck Institut für Astrophysik, Karl Schwarzshildstrasse 1, D-85748 Garching, Germany
[12] School of Physics and Astronomy, Tel Aviv University, Tel Aviv 69978, Israel
[13] Steward Observatory, 933 N. Cherry Ave., University of Arizona, Tucson, AZ 85721-0065, USA

Received ; accepted

ABSTRACT

Massive galaxies in the distant Universe form stars at much higher rates than today. Although direct resolution of the star forming regions of these galaxies is still a challenge, recent molecular gas observations at the IRAM Plateau de Bure interferometer enable us to study the star formation efficiency at sub-galactic scales around redshift $z = 1.2$. We present a method to obtain the gas and star formation rate (SFR) surface densities of ensembles of clumps composing galaxies at this redshift, even though the corresponding scales are not resolved. This method is based on the identification of these structures in position-velocity diagrams corresponding to slices within the galaxies. We use unique IRAM observations of the CO(3-2) rotational line and DEEP2 spectra of four massive star forming distant galaxies - EGS13003805, EGS13004291, EGS12007881 and EGS13019128 in the AEGIS terminology - to determine the gas and SFR surface densities of the identifiable ensembles of clumps that constitute them. The integrated CO line luminosity is assumed to be directly proportional to the total gas mass, and the SFR is deduced from the [OII] recombination line. We identify the ensembles of clumps with the angular resolution available in both CO and [OII] spectroscopy, i.e. 1-1.5". SFR and gas surface densities, $\Sigma_{\rm SFR}$ and $\Sigma_{\rm gas}$, are averaged in areas of this size, which is also the thickness of the DEEP2 slits and of the extracted IRAM slices, and we derive a spatially resolved Kennicutt-Schmidt (KS) relation at a scale of ~ 8 kpc. The data points globally follow a power law $\Sigma_{\rm SFR} \propto \Sigma_{\rm gas}^N$ of exponent N=1 corresponding to a depletion time of 1.0 Gyr, but with a large scatter, which means that the depletion time varies from point to point within the galaxies. We find a depletion time of 1.4±0.9 Gyr.

Key words. galaxies: evolution – galaxies: high redshift – galaxies: ISM – galaxies: starburst

1. Introduction

Ten billion years ago, between redshift 1 and 3, observed galaxies formed their stars at rates as high as ten times that of the Milky Way today (Noeske et al. 2007, Daddi et al. 2007). This implies a more abundent gas supply, either fueled by major mergers or by a semi-continuous gas accretion (Dekel et al. 2009, Dekel, Sari & Ceverino 2009). Recent observations of normal, massive, star-forming distant galaxies tend to show that most of these galaxies ($\geqslant$ 80%) are not experiencing major mergers or interactions (Tacconi et al. 2013), and that their light profiles are similar to those of their low redshift counterparts (Wuyts et al. 2011b). Also, the Kennicutt-Schmidt (KS) relation between total molecular gas and star formation rate (SFR) surface densities is nearly linear at all redshifts (Kennicutt 1998a, Wyder et al. 2009, Genzel et al. 2010, Tacconi et al. 2010), implying that the star formation processes seem to be largely independent of the cosmic epoch. The average fraction of molecular gas relative to the total baryonic mass must therefore have been up to ten times more at high redshift than in today's nearby galaxies, which is indeed corroborated by direct observations (Tacconi et al. 2013).

Numerical simulations suggest that typical massive star forming galaxies at high redshift continually accrete gas from the inter-galactic medium along cold and clumpy streams stemming from the cosmic web, while the disk fragments into a few clumps (Kereš et al. 2005, Bournaud & Elmegreen 2009, Dekel et al. 2009, Van de Voort et al. 2011). Galactic disks of distant galaxies are indeed found to be fragmented in a number of giant molecular clouds, or clumps, which differs from local galaxies, in which the molecular gas is scattered in numerous lower mass giant molecular clouds. The high-redshift star-forming complexes are found to have typical scales of ~1 kpc, masses up to 10^9 $M_\odot$, and contribute to 10-25% of the galaxy luminosity (Förster Schreiber et al. 2011). Most studies only consider averaged quantities for distant galaxies, as direct observations of the star-forming regions of high redshift galaxies are

⋆ e-mail: jonathan.freundlich@obspm.fr

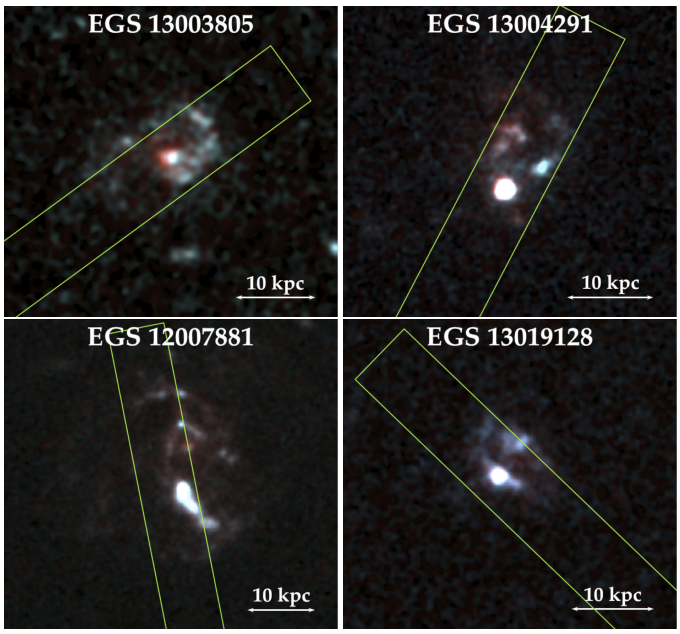

Fig. 1. Composite HST images of the four galaxies studied here, combining ACS I and V bands. The green box shows the DEEP2 slit used for each galaxy, whose size is indicated in Table 1 (Appendix). We assumed that the DEEP2 survey measured the position of the center of the galaxy more accurately than the HST, and shifted the HST image accordingly. North is up, east is left.

still challenging. KS relations have been derived at sub-galactic scales for nearby galaxies (Bigiel et al. 2008) but not yet extensively at high redshift.

In this letter, we use IRAM Plateau de Bure CO observations from the PHIBSS survey (Tacconi et al. 2013) and Keck DEEP2 spectra (Newman et al. 2012) of four massive galaxies at redshift $z \approx 1.2$ in order to investigate the star formation efficiency within their clumps, or groups of clumps. More precisely, our goal is to determine the SFR and the gas mass surface densities at sub-galactic scales and examine their correlation.

The four galaxies were drawn from the All-wavelength Extended Groth strip International Survey (AEGIS), which provides deep imaging in all major wave bands from X-rays to radio, including Hubble Space Telescope (HST) images, and optical spectroscopy (DEEP2/Keck) over a large area of sky (Noeske et al. 2007, Davis et al. 2007, Cooper et al. 2011, 2012, Newman et al. 2012), thus providing a complete set of galaxies between $0.2 \leqslant z \leqslant 1.2$. The four galaxies studied here were selected from the sample analyzed by Tacconi et al. 2010 and 2013, which gathered non major-merger, luminous, star forming galaxies at z~1.2, with stellar masses above 3. 10^{10} $M_\odot$ and SFR above 40 $M_\odot$ yr^{-1}. These four galaxies - named EGS13003805, EGS13004291, EGS12007881 and EGS13019128 in the AEGIS terminology - correspond to the massive end of the 'normal' star forming galaxies at z~1.2 (Tacconi et al. 2010). Figure 1 shows them in the I and V band of the HST Advanced Camera for Surveys (ACS), as well as the DEEP2 slits we used. To compute the physical distances, we adopt a cosmology with $\Omega_\Lambda = 0.73$, $\Omega_m = 0.27$, and $H_0 = 70$ km.s^{-1}.Mpc^{-1}.

2. Determination of the total gas mass and the SFR

2.1. The gas mass

We use high resolution observations of the CO(3-2) transition shifted into the 2 mm band for z~1.2 sources carried at the IRAM Plateau de Bure, including the most extended 'A' configuration. The angular resolution obtained is between 0.5" and 1.5" for all galaxies (Table 1 in Appendix), corresponding to physical scales between 4 and 13 kpc. The CO luminosity associated to any region of flux can be expressed as

$$\left(\frac{L'_{CO}}{K.km.s^{-1}.pc^2}\right) = 3.25\ 10^7\ (1+z)^{-3}\ \left(\frac{S_{CO}\Delta V}{Jy.km.s^{-1}}\right)\ \left(\frac{\nu_{obs}}{GHz}\right)^{-2}\ \left(\frac{D_L}{Mpc}\right)^2$$

where $S_{CO}\Delta V$ is the velocity integrated flux, ν_{obs} the observed frequency and D_L the luminosity distance (Solomon et al. 1997). To derive H_2 masses, we follow the approach used by Tacconi et al. 2010. This assumes a Milky Way like conversion factor of $\alpha = 3.2\ M_\odot\ (K\ km\ s^{-1}\ pc^2)^{-1}$ between the CO(1-0) luminosity and the H_2 mass, a factor 1.36 to account for interstellar helium, and a further correction by a factor 2 for the CO(3-2)/CO(1-0) luminosity ratio. The total gas masses of the four studied galaxies are indicated in Table 1 in the Appendix.

2.2. The star formation rate

Hα or [OII] recombination line luminosities are direct and sensitive tracers of young massive stars, and thus of the SFR (Kennicutt 1998b). Since the Hα line from the four galaxies considered here lies in the middle of a low atmospheric transmission band, ground-based Hα spectroscopy would be impossible, so we estimate the SFR from the [OII] recombination line (rest frame wavelength 3727 Å, shifted around 8200 Å for z~1.2 sources). We use spectra provided by the Keck DEEP2 survey, obtained with the high spectral resolution DEIMOS spectrograph (Faber et al. 2002) and taken along slits of typical size $5'' \times 1''$. The data was reduced using a dedicated pipeline (Newman et al. 2012, Cooper et al. 2012). A velocity resolution of about 50 km s^{-1} ($R = \lambda/\Delta\lambda \approx 5000$) enables to resolve the [OII] line (Davis et al. 2003). DEEP2 spectra are not flux calibrated and we use CFHT I band magnitudes (CFH12K camera) to calibrate the galaxy-integrated "1D" spectrum (Coil et al. 2004).

Even if the [OII] forbidden line luminosity is not directly coupled to the ionizing luminosity, it is possible to establish it empirically as a quantitative SFR tracer for the whole galaxy, and to express the SFR as

$$\left(\frac{SFR}{M_\odot.yr^{-1}}\right) = (5.3 \pm 1.5)\ 10^{-8}\ \left(\frac{L_{[OII]}}{L_\odot}\right)$$

where $L_{[OII]}$ is the [OII] line luminosity calculated from the galaxy-integrated "1D" spectrum (Kennicutt 1998b).

The values obtained for the SFR have to be corrected for dust extinction. The Galactic extinction is taken into account in the CFHT magnitudes, as they already include the dust corrections of Schlegel, Finkbeiner & Davis 1998, but the dust present in the galaxies themselves is an even larger cause of extinction. The above relationship between SFR and $L_{[OII]}$ was directly obtained from a similar Hα calibrated relation, so has only to be corrected with the Hα extinction, $A_{H\alpha}$ (Kennicutt 1998b). The dust distribution was derived from the SED of the galaxies, obtained from the B, R and I band CFHT magnitudes with the `kcorrect` software developed by Blanton & Roweis 2007 (version `v4_2`). The software provides SED curves with and without extinction, from which we can easily deduce $A_{H\alpha}$.

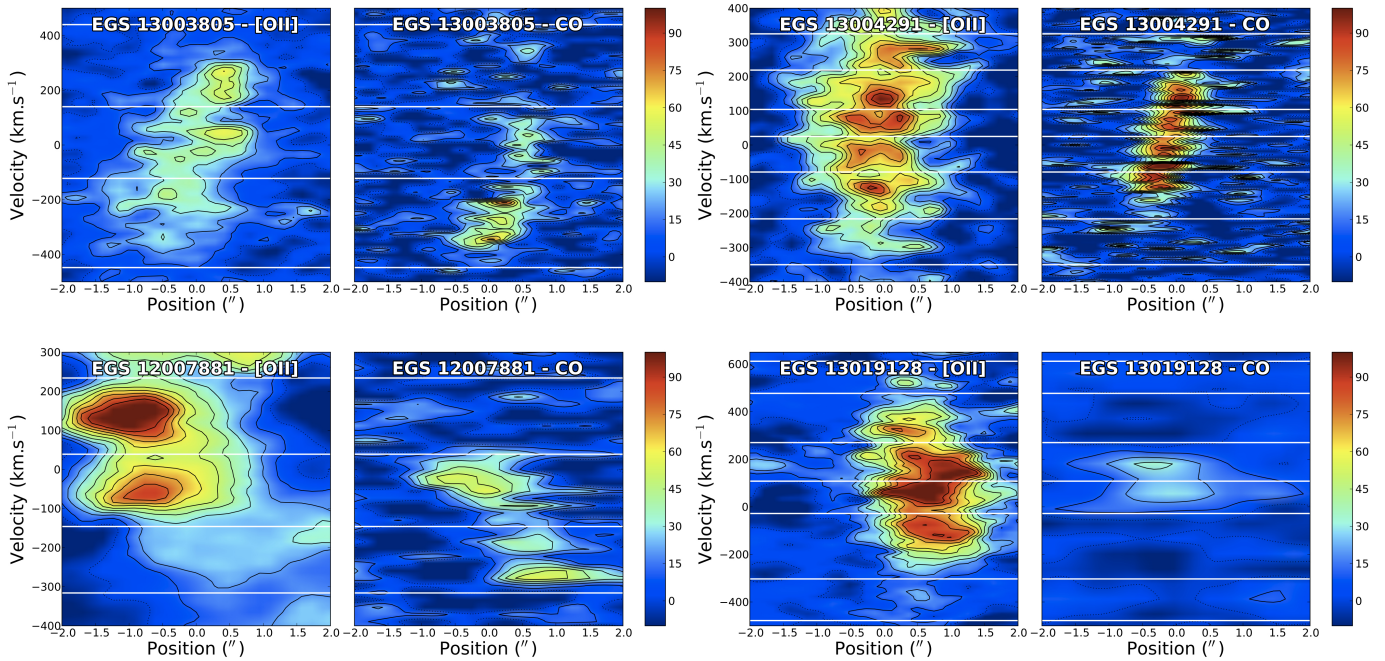

Fig. 2. [OII] line and CO luminosities (respectively left and right panels for each galaxy) in position-velocity planes corresponding to the DEEP2 slits. Smoothed ensembles of clumps are separated by eye along the vertical axis, as shown with the white horizontal lines. The [OII] diagrams were normalized in order to have fluxes proportional to the SFR, but all galaxies share the same arbitrary color scales. One arcsecond corresponds approximately to 8.5 kpc (Table 1 in the Appendix).

The obtained extinctions are coherent with predicted extinction ratios (O'Donnell 1994) and observations (e.g. Förster Schreiber et al. 2011), but the inferred SFR (Table 1 in Appendix) differ up to 3σ from the values obtained by Tacconi et al. 2013. These latter values derived from UV and Spitzer 24 μm luminosities, with the methods of Wuyts et al. 2011a, give the same orders of magnitude, but have a larger scatter for the four galaxies considered here. The empirical calibration through B-band luminosity presented by Moustakas et al. 2006 gives different values as well, the three methods being subject to comparable uncertainties and none of them being clearly better than the others. The SFR obtained by Tacconi et al. 2013 and through Moustakas et al. 2006 B-band calibration are given for information in Table 1 (Appendix), but would both increase the scatter in the resulting sub-galactic KS diagram without significantly changing our conclusions.

3. A resolved Kennicutt-Schmidt law

HST images of Figure 1 reveal kpc-sized clumps within diffuse regions, but these clumpy features (~ 0.1") are smoothed out at DEEP2 and IRAM resolutions, whose ranges are respectively 0.6-1.0" and 0.5-1.6". Spectroscopy, however, helps to separate different components, thanks to their kinematics. DEEP2 spectra correspond to position-velocity diagrams (PV diagrams) along the galaxy major axis (Davis et al. 2007). Figure 2 compares the [OII] position-velocity diagrams with the corresponding slices in CO(3-2), both with the same 1" width. Smoothed 1"-sized ensembles of clumps are separated by eye along the velocity axis of the PV diagrams. The characteristics of these ensembles are given in Table 2 (Appendix), and we aim at describing the star formation efficiency within them. We tried to compensate the substructure separation by eye by taking into account all identifiable ensembles of clumps.

From the CO and [OII] lines, we estimate the gas mass and the SFR contained in areas of 1" in diameter (corresponding to the width of the slice and approximately to the size of the ensembles of clumps), and obtain the corresponding averaged surface densities, $\Sigma_{\rm gas}$ and $\Sigma_{\rm SFR}$. The resulting KS diagram is displayed in Figure 3. The data points scatter around the line of slope N=1 corresponding to a depletion time ($t_{\rm depl}$ = $M_{\rm gas}$/SFR) of 1.0 Gyr, but this latter quantity is locally very different from one data point to the other. As shown in Figure 4, the mean depletion time is 1.4 Gyr, with a standard deviation of 0.9 Gyr, as compared for whole galaxies to 2.0±0.8 Gyr at z=0 in Bigiel et al. 2008, 0.5-1.5 Gyr from z~2 to z~0 in Genzel et al. 2010 and ~0.7 Gyr at z=1-3 in Tacconi et al. 2013. Our sample is too incomplete to compute a best fit slope, but the method developed here could be applied to more high redshift galaxies.

4. Discussion and conclusion

4.1. Advantages of the method

We have shown how the various ensembles of clumps can be separated by their kinematics in PV diagrams, even though the angular resolution of molecular gas and SFR data was not able to separate them in integrated intensity. As such, the KS diagram can be obtained within regions of the resolution size (~1").

Previous resolved KS work at high redshift was only obtained using serendipitous amplification by gravitational lenses. Decarli et al. 2012 carried out one of the first spatially resolved studies in high redshift galaxies, using [NII], FIR and CO observations for two gravitationally lensed z~3.9 galaxies. They obtain a steep relation of slope N = 1.4 ±0.2 between the dust continuum and the molecular gas surface brightness. Strong lenses are rare, and the determination of the clumps physical parameters depend on the lensing model. Our method is probably more

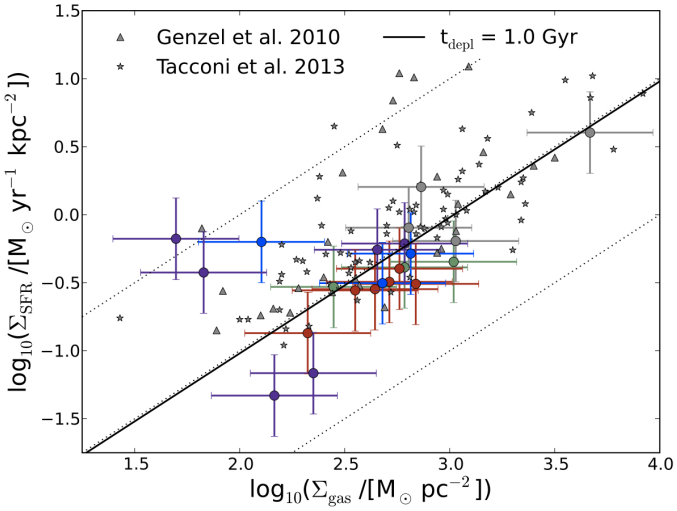

Fig. 3. Kennicutt-Schmidt diagram for 1" ensembles of clumps of EGS13003805 (green), EGS13004291 (red), EGS12007881 (blue) and EGS13019128 (purple), also displaying data points for these four galaxies as a whole (grey). The dotted diagonal lines correspond to constant gas depletion times of 0.1, 1, and 10 Gyr from top to bottom, and the solid black line to the best linear fit with an N=1 slope for the sub-galactic features. The corresponding depletion time is t_{depl}=1.0 Gyr. The error bars of 0.3 dex yield a reduced χ^2 close to 1. The grey data points are taken from Genzel et al. 2010 and Tacconi et al. 2013.

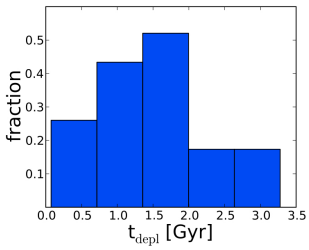

Fig. 4. Distribution of depletion time scales for the 16 regions identified in the four galaxies studied in this letter. The distribution has a mean of t_{depl} = 1.4 Gyr and a standard deviation of 0.9 Gyr.

appropriate for a systematic study of the star formation at high redshift, until higher resolution instruments resolve the clumps.

In the absence of high-resolution molecular gas data, Swinbank et al. 2012 report adaptive optics Hα observations of eleven kpc-scale star forming regions identified in $z = 0.84-2.23$ galaxies and measure the velocity dispersion of the ionized gas σ and the star formation surface density Σ_{SFR}. By assuming that σ also corresponds to the dispersion of the cold clumps and that the clumps are marginally stable with a Toomre parameter $Q \simeq 1$, they claim a correlation between the gas surface density Σ_{gas} and Σ_{SFR}. But the method is highly indirect, relies on many assumptions, and underestimates beam smearing effects in the determination of σ.

4.2. Biases and uncertainties

The four galaxies studied here are particularly luminous, and were selected from a sample (Tacconi et al. 2010) with stellar masses and star formation rates respectively higher than 3. 10^{10} $M_\odot$ and 40 $M_\odot$ yr^{-1}. A high luminosity was also needed to visualize and isolate the clumps in the PV diagrams, so this method is intrinsically biased towards massive galaxies.

The main uncertainties to estimate gas and SFR surface densities come from the values used for $\alpha = M_{H_2}/L'_{CO}$, for the CO(3-2)/CO(1-0) luminosity ratio, and for the extinction $A_{H\alpha}$. These quantities could vary significantly from one galaxy to the other, and would cumulatively infer multiplicative factors as high as 2 or 3 in our final values for the mass of gas and of the SFR.

4.3. Conclusion

Our results, as well as most other observations (Genzel et al. 2010, Tacconi et al. 2010, Tacconi et al. 2013, Decarli et al. 2012, Swinbank et al. 2012), indicate that the star formation scaling law between SFR and gas surface densities is not significantly different at high redshift than in the local Universe. Our limited sample of ~8 kpc-scale ensembles of clumps of distant galaxies is compatible with a power law $\Sigma_{SFR} \propto \Sigma_{gas}^N$ of exponent N=1 and a depletion time of 1.0 Gyr, which is of the same order of magnitude as measurements at lower redshift. This adds to the growing evidence that the star formation processes ten billions years ago were similar to the ones that are observed in the local Universe. The method developed here could be applied to a more significant sample of high redshift galaxies, to obtain more statistically robust results.

Acknowledgements. J. Freundlich acknowledges support by the École Normale supérieure (ENS, Paris), and is thankful to Philippe Salomé for numerous technical tips and Martin Stringer for his proofreading and suggestions. This work is based on observations carried out with the IRAM Plateau de Bure Interferometer. IRAM is supported by INSU/CNRS (France), MPG (Germany) and IGN (Spain). This work also makes use of data from AEGIS, a multiwavelength sky survey conducted with the Chandra, GALEX, Hubble, Keck, CFHT, MMT, Subaru, Palomar, Spitzer, VLA, and other telescopes and supported in part by the NSF, NASA, and the STFC.

References

Bigiel, F., Leroy, A., Walter, F., et al., 2008, ApJ, 136, 2846
Blanton, M. R., & Roweis, S., 2007, ApJ, 133, 734
Bournaud, F., & Elmegreen, B. C., 2009, ApJ, 694, L158
Coil, A. L., Newman, J. A., Kaiser, N., et al., 2004, ApJ, 617, 765C
Cooper, M. C., Aird, J. A., Coil, A. L., 2011, ApJS, 193, 14C
Cooper, M. C., Newman, J. A., Davis, M., et al., 2012, ASCL, 1203.003
Daddi, E., Dickinson, M., Morrison, G., et al., 2007, ApJ, 670, 156
Davis, M., Faber, S. M., Newman, J. A., et al., 2003, Proc. SPIE, 4834, 161
Davis, M., Guhathakurta, P., Konidaris, N. P., et al., 2007, ApJ, 660, L1
Decarli, R., Walter, F., Neri, R., et al., 2012, ApJ, 752, 2D
Dekel, A., Birnboim, Y., Engel, G., et al., 2009, Nature, 457, 451D
Dekel, A., Sari, R., & Ceverino, D., 2009, ApJ, 703, 785
Dickman, R. L., Snell, R. L., & Schoerb, F. P., 1986, ApJ, 309, 326
Faber, S. M., Phillips, A. C., Kibrick, R. I., et al. 2002, Proc. SPIE, 4841, 1657
Förster Schreiber, N. M., Shapley, A. E., Genzel, R., et al., 2011, ApJ, 739, 45F
Genzel, R., Tacconi, L. J., Gracia-Carpio, J., et al., 2010, MNRAS, 407, 2091
Kennicutt, R. C. Jr., 1998a, ApJ, 498, 541
Kennicutt, R. C. Jr., 1998b, ARA&A, 36, 189
Kereš, D., Katz, N., Weinberg, D. H., & Davé, R., 2005, MNRAS, 363, 2K
Moustakas, J., Kennicutt, R. C., & Tremonti, C., 2006, ApJ, 642, 775M
Newman, J. A., Cooper, M. C., Davis, M., et al., 2012, submitted to ApJS
Noeske, K. G., Weiner, B. J., Faber, S., et al., 2007, ApJ, 660, L43
O'Donnell, J. E., 1994, ApJ, 422, 158
Schlegel, D., Finkbeiner, D., & Davis, M., 1998, ApJ, 121, 161
Solomon, P. M., Downes, D., Radford, S. J. E., et al., 1997, ApJ, 478, 144
Solomon, P. M., Rivolo, A. R., Barrett, J., et al., 1987, ApJ, 319, 730
Swinbank, A. M., Smail, I., Sobral, D., et al., 2012, submitted to ApJ
Tacconi, L. J., Genzel, R., Neri, R., et al., 2010, Nature, 463, 781T
Tacconi, L. J., Neri, R., Genzel, R., et al., 2013, submitted to ApJ
Van de Voort, F., Schaye, J., Booth, C. M., et al., 2011, MNRAS, 414, 2458
Wyder, T. K., Martin, D. C., Barlow, T. A., et al., 2009, ApJ, 696, 1834W
Wuyts, S., Förster Schreiber, N., Lutz, D., et al., 2011, ApJ, 738, 106
Wuyts, S., Förster Schreiber, N. M., van der Wel, A., et al., 2011, ApJ, 742, 96W

Table 1. Some global properties and observational details for the four galaxies studied in this letter: (1) the redshift, as determined in the AEGIS catalogues from the [OII] line using DEEP2 spectra ; (2) the angular distance D_A and the luminosity distance D_L ; (3) the gas mass derived from the IRAM Plateau de Bure observations ; (4) the SFR from the [OII] line luminosity in the galaxy-integrated "1D" spectrum, obtained according to section 2.2 ; (5) the total star mass obtained by SED fittings from CFHT B, R, and I bands photometric data using `kcorrect` (Blanton & Roweis 2007), corrected for a Universe with $H_0 = 70$ km.s^{-1}.Mpc^{-1} ; (6) the gas fraction $f_{gas} = M_{gas}/(M_{gas} + M_{star})$; (7) the optical half light radius $R_{1/2}$ as indicated in Tacconi et al. 2013 ; (8) the surface densities associated to the gas mass, the star formation rate and the star mass, calculated within $R_{1/2}$, for example as $\Sigma_{gas} = 0.5\ M_{gas}/\pi R_{1/2}^2$; (9) Hα, visible and [OII] extinctions as derived from the `kcorrect` SED reconstruction ; (10) the extinction-corrected SFR obtained from 24 μm and UV continuum by Tacconi et al. 2013 ; and (11) the SFR ψ extrapolated from the empirical calibration of Moustakas et al. 2006 (section 4.3). A_V, $A_{[OII]}$, $SFR_{24\mu m+UV}$ and ψ are given for information only. The comparison between the SFR obtained according to section 2.2, $SFR_{24\mu m+UV}$ and ψ gives an idea of the uncertainties in the SFR. Using $SFR_{24\mu m+UV}$ from Tacconi et al. 2013 would give a constant depletion time linear fit with $t_{depl} = 1.1$ Gyr and values for t_{depl} between 0.6 and 10.3 Gyr (mean 2.1 Gyr), whereas using ψ calibrated through Moustakas et al. 2006 would give a fit with $t_{depl} = 1.2$ Gyr and t_{depl} between 1.6 and 4.2 Gyr (mean 1.8 Gyr).

Properties	EGS 13003805	EGS 13004291	EGS 12007881	EGS 13019128
z (1)	1.2318	1.19705	1.16105	1.3494
D_A [Mpc] (2)	1753.0	1745.3	1736.4	1772.8
D_L [Mpc] (2)	8731.5	8424.7	8108.8	9785.1
Scale [kpc/"]	8.50	8.46	8.42	8.60
DEEP2 slit size	$6.863'' \times 1''$	$5.149'' \times 1''$	$5.762'' \times 1''$	$10.343'' \times 1''$
DEEP2 slit orientation (PA)	$-53.858°$	$-27.649°$	$11.142°$	$46.142°$
IRAM CO(3-2) beam	$0.8'' \times 0.6''$	$0.6'' \times 0.5''$	$1.1'' \times 0.9''$	$1.6'' \times 1.4''$
M_{gas} [10^{11} $M_\odot$] (3)	2.2	2.8	1.3	1.2
SFR [$M_\odot$ yr^{-1}] (4)	131	242	164	272
M_{star} [10^{11} $M_\odot$] (5)	3.4	5.0	5.0	3.8
f_{gas} (6)	0.39	0.36	0.21	0.24
$R_{1/2}$ [kpc] (7)	5.7	3.1	5.7	5.2
$\log_{10}(\Sigma_{gas}/[M_\odot pc^{-2}])$ (8)	3.03	3.67	2.80	2.86
$\log_{10}(\Sigma_{SFR}/[M_\odot yr^{-1} kpc^{-2}])$ (8)	-0.193	0.604	-0.095	0.204
$\log_{10}(\Sigma_{star}/[M_\odot pc^{-2}])$ (8)	3.22	3.92	3.39	3.36
$A_{H\alpha}$ (9)	1.25	1.28	1.06	1.21
A_V (9)	1.56	1.60	1.30	1.50
$A_{[OII]}$ (9)	2.28	2.26	2.04	2.19
$SFR_{24\mu m+UV}$ [$M_\odot$ yr^{-1}] (10)	200	630	94	87
ψ [$M_\odot$ yr^{-1}] (11)	63	231	265	213

Table 2. Some properties of the clumps of EGS 13004291, EGS 13003805, EGS 12007881 and EGS 13019128 obtained from measurements in the position-velocity diagrams: (1) the gas mass obtained as a fraction of the total mass of the galaxy from the CO position-velocity diagram: (2) the SFR obtained similarly from the [OII] position-velocity diagram, normalized with the total SFR determined according to section 2.2 ; (3) the derived gas mass and SFR surface densities averaged over the same area of 1" in diameter ; (4) the depletion time $t_{depl} = M_{gas}/SFR$; and (5) the FWHM obtained from the IRAM position-velocity diagram with a gaussian fit in the direction of the slice (for information only). The FWHM roughly corresponds to the IRAM beam size, so we preferred to use the same 1" size for all clumps in the different calculations. Using the FWHM instead of a constant 1" diameter to calculate the surface densities gives a much larger scatter, but actually does not change the constant depletion time fit and the values of t_{depl}. The clumps are numbered from bottom to top according to the horizontal separation lines of Figure 2.

Clump	M_{gas} [10^{10} $M_\odot$] (1)	SFR [$M_\odot.yr^{-1}$] (2)	$\log_{10}\left(\frac{\Sigma_{gas}}{M_\odot.pc^{-2}}\right)$ (3)	$\log_{10}\left(\frac{\Sigma_{SFR}}{M_\odot.yr^{-1}.kpc^{-2}}\right)$ (3)	t_{depl} [Gyr] (4)	FWHM ["] (5)
EGS 13003805-I	11.85	51.17	3.019	−0.346	2.32	0.93
EGS 13003805-II	6.92	46.52	2.785	−0.387	1.49	0.78
EGS 13003805-III	3.18	33.45	2.447	−0.531	0.95	0.63
EGS 13004291-I	2.37	15.15	2.324	−0.870	1.56	0.78
EGS 13004291-II	5.80	36.10	2.713	−0.494	1.61	0.64
EGS 13004291-III	7.75	34.88	2.838	−0.508	2.22	0.74
EGS 13004291-IV	4.96	31.89	2.644	−0.547	1.55	0.79
EGS 13004291-V	6.28	45.10	2.761	−0.397	1.44	0.61
EGS 13004291-VI	3.99	31.26	2.550	−0.556	1.28	1.1
EGS 12007881-I	5.33	34.94	2.680	−0.503	1.52	1.35
EGS 12007881-II	7.26	57.64	2.814	−0.286	1.26	1.36
EGS 12007881-III	1.41	70.27	2.10	−0.200	0.20	1.57
EGS 13019128-I	1.70	5.43	2.165	−1.330	3.12	0.83
EGS 13019128-II	0.58	77.22	1.697	−0.177	0.07	1.14
EGS 13019128-III	7.08	71.22	2.785	−0.212	0.99	1.67
EGS 13019128-IV	5.25	64.10	2.655	−0.258	0.82	1.60
EGS 13019128-V	0.78	43.61	1.828	−0.425	0.18	1.62
EGS 13019128-VI	2.60	7.94	2.351	−1.165	3.28	1.86